

This is a repository copy of *The formation of atomic oxygen and hydrogen in atmospheric pressure plasmas containing humidity:picosecond two-photon absorption laser induced fluorescence and numerical simulations.*

White Rose Research Online URL for this paper:

<https://eprints.whiterose.ac.uk/id/eprint/162528/>

Version: Published Version

Article:

Schröter, Sandra orcid.org/0000-0003-1029-4041, Bredin, Jérôme, Gibson, Andrew R. orcid.org/0000-0002-1082-4359 et al. (6 more authors) (2020) The formation of atomic oxygen and hydrogen in atmospheric pressure plasmas containing humidity:picosecond two-photon absorption laser induced fluorescence and numerical simulations. Plasma Sources Science and Technology. 105001. ISSN: 0963-0252

<https://doi.org/10.1088/1361-6595/abab55>

Reuse

This article is distributed under the terms of the Creative Commons Attribution (CC BY) licence. This licence allows you to distribute, remix, tweak, and build upon the work, even commercially, as long as you credit the authors for the original work. More information and the full terms of the licence here:

<https://creativecommons.org/licenses/>

Takedown

If you consider content in White Rose Research Online to be in breach of UK law, please notify us by emailing eprints@whiterose.ac.uk including the URL of the record and the reason for the withdrawal request.

PAPER • OPEN ACCESS

The formation of atomic oxygen and hydrogen in atmospheric pressure plasmas containing humidity: picosecond two-photon absorption laser induced fluorescence and numerical simulations

To cite this article: Sandra Schröter *et al* 2020 *Plasma Sources Sci. Technol.* **29** 105001

View the [article online](#) for updates and enhancements.



IOP | ebooks™

Bringing together innovative digital publishing with leading authors from the global scientific community.

Start exploring the collection—download the first chapter of every title for free.

The formation of atomic oxygen and hydrogen in atmospheric pressure plasmas containing humidity: picosecond two-photon absorption laser induced fluorescence and numerical simulations

Sandra Schröter¹, Jérôme Bredin^{1,4}, Andrew R Gibson^{1,2,3}, Andrew West^{1,5}, James P Dedrick¹, Erik Wagenaars¹, Kari Niemi¹, Timo Gans¹ and Deborah O'Connell^{1,*}

¹ York Plasma Institute, Department of Physics, University of York, Heslington, York YO10 5DD, United Kingdom

² Research Group for Biomedical Plasma Technology, Ruhr-Universität Bochum, Universitätsstraße 150, 44801 Bochum, Germany

³ Institute of Electrical Engineering and Plasma Technology, Ruhr-Universität Bochum, Universitätsstraße 150, 44801 Bochum, Germany

E-mail: deborah.oconnell@york.ac.uk

Received 3 April 2020, revised 28 July 2020

Accepted for publication 31 July 2020

Published 15 October 2020



Abstract

Atmospheric pressure plasmas are effective sources for reactive species, making them applicable for industrial and biomedical applications. We quantify ground-state densities of key species, atomic oxygen (O) and hydrogen (H), produced from admixtures of water vapour (up to 0.5%) to the helium feed gas in a radio-frequency-driven plasma at atmospheric pressure. Absolute density measurements, using two-photon absorption laser induced fluorescence, require accurate effective excited state lifetimes. For atmospheric pressure plasmas, picosecond resolution is needed due to the rapid collisional de-excitation of excited states. These absolute O and H density measurements, at the nozzle of the plasma jet, are used to benchmark a plug-flow, 0D chemical kinetics model, for varying humidity content, to further investigate the main formation pathways of O and H. It is found that impurities can play a crucial role for the production of O at small molecular admixtures. Hence, for controllable reactive species production, purposely admixed molecules to the feed gas is recommended, as opposed to relying on ambient molecules. The controlled humidity content was also identified as an effective tailoring mechanism for the O/H ratio.

Keywords: atmospheric-pressure plasma jet, two-photon absorption laser induced fluorescence (TALIF), plasma chemistry, reactive species, radio-frequency driven plasma, humidity admixtures

⁴Current affiliation: Tokamak Energy Ltd, 173 Brook Drive, Milton Park OX14 4SD, United Kingdom.

⁵Current affiliation: Department of Electrical and Electronic Engineering, The University of Manchester, Manchester M13 9PL, United Kingdom.

*Author to whom any correspondence should be addressed.



Original content from this work may be used under the terms of the [Creative Commons Attribution 4.0 licence](https://creativecommons.org/licenses/by/4.0/). Any further distribution of this work must maintain attribution to the author(s) and the title of the work, journal citation and DOI.

(Some figures may appear in colour only in the online journal)

1. Introduction

Non-thermal atmospheric pressure plasma jets (APPJs) driven with radio-frequency (rf) power are very efficient sources of reactive species [1–10]. Reactive species play a crucial role in applications such as surface treatment [11–13], etching [14–16] and biomedicine [17–22]. APPJs enable the localised delivery of reactive species to temperature sensitive biological samples [21, 23]. They have therefore generated considerable interest with respect to medical applications including wound healing [24–28] and cancer therapies [29–36]. A key feature of APPJs is their potential to enhance treatment through the synergistic delivery of multiple reactive species, and other plasma components. To achieve optimised reactive species delivery, and treatment effectiveness, for a given application, it is crucial to understand the mechanisms behind the formation of important reactants and the chemical kinetics that occur both in the plasma itself and the plasma effluent, which is in direct contact with the treated sample.

Atomic species, such as atomic oxygen, hydrogen, and nitrogen (O, H, and N), are very reactive and are important precursors for longer lived species, such as nitrogen oxides N_xO_y , or ozone, which can play an important role in, for example, biomedical applications [1]. Therefore, their precise quantification in the plasma effluent region is crucial in understanding underlying fundamental mechanisms, which can then help to optimise parameters such as gas composition and treatment time. The quantification of reactive species in APPJs meets many challenges naturally arising from the geometry and characteristics of these sources when compared to low-pressure systems. Dimensions of APPJs are typically small, in the order of μm to mm, requiring a high spatial resolution of the diagnostics that are used for the quantification of reactive species. On the other hand, the strong collisionality in APPJs can significantly reduce lifetimes of excited states in a radiation-less manner (quenching), posing additional challenges.

An established diagnostic technique for quantifying atomic species such as O, H, and N is two-photon absorption laser induced fluorescence (TALIF) [37–45]. TALIF measurements can provide high spatial resolution, in contrast to other techniques, such as for example absorption spectroscopy, which is typically used to measure line-of-sight averaged densities. TALIF is based on the measurement of fluorescence emission from a laser-excited state, which depends on all de-population mechanisms of that particular state, such as radiative de-excitation and radiation-less collisional quenching. Particularly the latter process can lead to a strong reduction of both the absolute fluorescence signal and the lifetime of the laser excited state at atmospheric pressure. Most conventional TALIF systems used for the investigations of APPJs comprise lasers and detection systems that operate with timescales in the region of nanoseconds, and are therefore not able to temporally resolve the excited state lifetime at elevated pressures. Although this can be calculated using quenching coefficients from the literature, e.g. [46–48], uncertainties can

be introduced due to the uncertainties associated with the rate coefficients for these processes, or because the gas mixture is complex and the distribution of quenching partners unknown. The latter is particularly the case for plasma effluents of APPJs, where a gradual mixing of the feed gas with the background gas takes place, which typically is ambient air. Bruggeman *et al* use direct measurement of gas temperatures and computational fluid dynamics modelling to take these effects into account [49–51]. Nevertheless, the use of nanosecond TALIF for the quantification of atomic species can be challenging in these complex systems, where the use of faster laser systems and detector in the picosecond or femtosecond temporal range offers a clear advantage [52–55].

In this paper, TALIF measurements of O and H atom densities in an APPJ (COST- μ APPJ [56]) in a mixture of helium (He) with small amounts of humidity (H_2O) using a tunable picosecond (ps) laser system are presented. The enhanced temporal resolution (compared to conventional ns-laser systems) allows us to directly determine the effective collisional-induced quenching rate of the laser-excited states. Therefore, absolute densities of ground state O and H atoms can be determined without knowledge of the collisional dominated ambient environment at atmospheric pressure.

We compare measured O and H densities with values calculated with a zero-dimensional plasma-chemical kinetics model. The reaction mechanism has been introduced in previous work [57]. After obtaining good qualitative and quantitative agreement of absolute densities between simulation and experiments, we use the simulation to further investigate the plasma chemical kinetics, such as formation pathways for O and H, as well as the role of oxygen containing impurities on the plasma chemistry.

2. Experimental setup

2.1. Atmospheric pressure plasma jet

The APPJ investigated in this work is similar to the COST- μ APPJ, which is described in reference [56]. The plasma is ignited in a gas channel of $1 \times 1 \text{ mm}^2$ cross section and 30 mm length, which is confined by two stainless steel electrodes and two quartz windows from the gas inlet to the exit nozzle. One of these electrodes is powered by applying rf voltage (frequency 13.56 MHz) using a power generator (Coaxial Power Systems RFG-50-13) and an impedance matching unit (Coaxial Power Systems MMN-150-13), while the other is grounded. In this work, we apply a peak-to-peak voltage of 510 V, which is monitored using a high voltage probe (PMK, PPE20KV, 100 MHz). At these low voltages, the plasma operates in Ω mode [58]. In contrast to the COST- μ APPJ, the plasma source used in this work does not contain the internal resonance coupler described in [56] (section 3.2). However, the critical dimensions and operating conditions of both sources are practically the same.

Gas is introduced into the confined discharge channel, and exits at the nozzle into open air. High purity He (99.996% purity) at a flow of 0.5 slm serves as a buffer gas, and water vapor of up to 0.5% (5000 ppm) can be admixed in order to create reactive species due to dissociation of these H₂O molecules. The flow rate is chosen to match the conditions of earlier work [57], where a ten times higher gas flow was used in a plasma source with an approximately ten times larger cross sectional area compared to the COST-μAPPJ. For He, the gas flow is regulated by using two mass flow controllers, as described in earlier work [57]. One of the two branches is guided through a bubbler, which consists of a 120 cm long domed glass adapter (Biallec GmbH) that is clamped to a KF40 flange with inlet and outlet tubes, as described previously [57]. The flows of dry and humidified He are combined and fed into the discharge channel. Assuming that the He is saturated with water vapour after passing through the bubbler, the total amount of water in the vapour phase can be calculated using the vapour pressure $p_{\text{H}_2\text{O}}^{\text{vap}}$ of H₂O [59] and the flow rate of the He through the bubbler $F_{\text{He}}^{\text{bubbler}}$, as has been described elsewhere [60]:

$$p_{\text{H}_2\text{O}}^{\text{vap}} = 6.112 \times 10^{-3} \exp\left(\frac{17.62T_w}{243.12 + T_w}\right) \text{ bar}, \quad (1)$$

$$F_{\text{H}_2\text{O}} = F_{\text{He}}^{\text{bubbler}} \frac{p_{\text{H}_2\text{O}}^{\text{vap}}}{p_{\text{atm}} - p_{\text{H}_2\text{O}}^{\text{vap}}}, \quad (2)$$

where T_w is the water temperature in °C. For some of the measurements carried out here, the bubbler was immersed in a water bath which was regulated at 18°C. It will be clarified in each section for which measurements the water cooling has been applied.

2.2. Picosecond two-photon absorption laser induced fluorescence

2.2.1. Absolute density calibration.

For quantifying the absolute atomic oxygen and hydrogen densities n_x , we measure the spatially, temporally, and spectrally integrated fluorescence signal S_F , and compare its intensity with the fluorescence signal obtained from a noble gas of a known quantity. For the calibration measurement, the plasma source is replaced with a Starna Spectrosil Fluorometer Cuvette, which is filled with the respective noble gas (xenon or krypton) at defined pressures (10 Torr for Xe and 1 Torr for Kr).

For the further discussion, the following abbreviations are used when mentioning different states: ‘O’ for the ground states $\sum_J \text{O}(2p^4 \ ^3P_J)$ and ‘H’ for the $\text{H}(1s \ ^2S_{1/2})$ ground state. The excited states are abbreviated as O* for the $\sum_J \text{O}(3p \ ^3P_J)$ [or short: O(3p ³P)], and as H* for the $\text{H}(n = 3)$ state.

A comparison of the fluorescence intensities yields absolute densities for the species of interest

$$\frac{S_{F,x}}{S_{F,\text{cal}}} = \frac{\eta(\lambda_{F,x})}{\eta(\lambda_{F,\text{cal}})} \frac{T_f(\lambda_{F,x})}{T_f(\lambda_{F,\text{cal}})} \frac{1}{T_c(\lambda_{F,\text{cal}})} \frac{a_{ik,x}}{a_{ik,\text{cal}}} \frac{\sigma_x^{(2)}}{\sigma_{\text{cal}}^{(2)}} \frac{n_x}{n_{\text{cal}}} \times \left(\frac{E_x}{E_{\text{cal}}/T_c(\lambda_{L,\text{cal}})} \frac{\lambda_{L,x}}{\lambda_{L,\text{cal}}} \right)^2. \quad (3)$$

Here, λ is the wavelength of either the laser (L) or fluorescence (F) radiation for the species of interest ($x = \text{O}, \text{H}$) and calibration species ($\text{cal} = \text{Xe}, \text{Kr}$), T_c is the single-wall transmission of the calibration cuvette, T_f the transmission of the interference filter placed in front of the camera for the respective wavelength, $\sigma^{(2)}$ the two-photon excitation cross section, and E the laser pulse energy. In our case, the required laser pulse energy inside the calibration cuvette is expressed as $E_{\text{cal}}/T_c(\lambda_{L,\text{cal}})$, since E_{cal} was measured behind (not in front of) the calibration cuvette. If the laser-excited, fluorescent state is denoted by the letter i , then a_{ik} denotes the branching ratio of the transition into the lower state k

$$a_{ik} = \frac{A_{ik}}{\sum_k A_{ik} + \sum_q k_q^i n_q} = \frac{A_{ik}}{A_i + Q_i} = \frac{A_{ik}}{A_i} \frac{A_i}{A_i + Q_i} = b_{ik} \frac{\tau_{\text{eff}}}{\tau_{\text{nat}}}. \quad (4)$$

A_{ik} is the decay rate for the transition from state i to k , while the inverse of the sum of decay rates into all possible lower states k is the natural lifetime $\tau_{\text{nat}} = (\sum_k A_{ik})^{-1}$ of the state i . The natural lifetimes for O*, H*, Xe(6p'[3/2]₂), and Kr(5p'[3/2]₂) are 34.7 ns, 17.6 ns, 40.8 ns, and 34.1 ns, respectively, according to [61, 62]. b_{ik} is the purely optical branching ratio into a specific state k , and τ_{eff} the effective lifetime of the laser excited state. The effective lifetime takes into account both the natural lifetime of the excited state, as well as radiationless collisional de-excitation (quenching) via collisions of the excited states with the background gas, which can significantly lower the excited state lifetime. Quenching is dependent on quenching coefficients k_q and densities n_q of the quenching species.

Comprising all instrumental constants into one overall calibration constant C , equation (3) can be further simplified to

$$n_x = C \frac{\tau_{\text{eff, cal}}}{\tau_{\text{eff, x}}} \frac{S_{F,x}}{S_{F,\text{cal}}} n_{\text{cal}}, \quad (5)$$

where S_F and τ_{eff} are the measurable quantities.

The established calibration schemes for O and H using Xe and Kr [61, 62] are shown in figure 1 including the emission and fluorescence wavelengths, and purely optical branching ratios b_{ik} . Data for the schematics have been taken from other publications [61, 62] and the NIST Atomic Spectra Database [63].

The calibration schemes are chosen in a way such that both the excitation and fluorescence wavelengths for the species of interest and calibration species are close, to prevent any influence of changes in transmission or beam profile due to optics used to guide the laser beam. The schematics presented in figure 1 have been discussed in much detail in previous work [39, 53, 64, 65], and only the main aspects will be discussed here.

In *atomic oxygen*, both the ground and the TALIF excited state (O(2p⁴ ³P_J) and O(3p ³P_J), respectively) are split into three energy sub-levels $J = 0, 1, 2$. While the ground state levels have a distinct energy gap in the order of a few hundred wavenumbers, the upper states lie energetically very close, i.e. within one wavenumber. Therefore, excitation from one of the ground state levels can populate all three $J = 0, 1, 2$ upper state

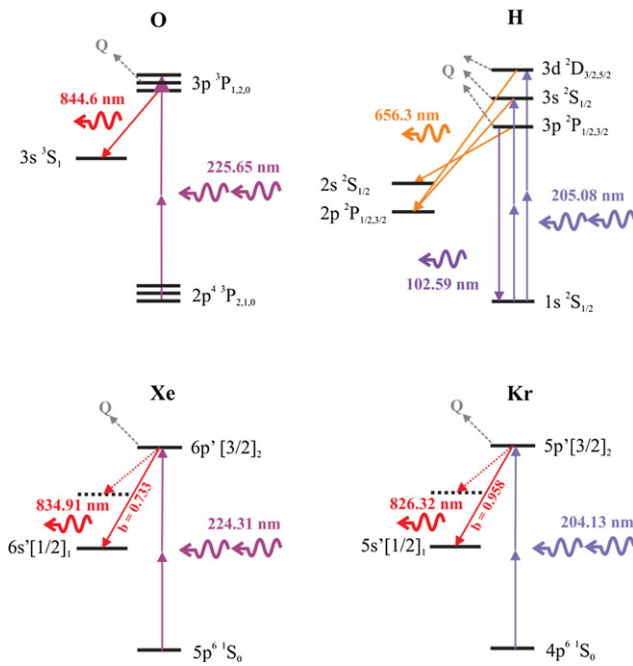


Figure 1. TALIF schemes for the investigated species O and H and corresponding calibration gases, which are Xe and Kr, respectively.

levels, if optically allowed, because their splitting is within the spectral width of the laser used in this work (about 4 cm^{-1}).

Xenon is typically chosen as a calibration gas for O, since both the excitation and fluorescence wavelengths are in close proximity. The excited Xe state can decay into several sub-levels. b_{ik} for the transition into the 6s state with a wavelength of 834.9 nm is 0.733 [66].

In this work, the following two-photon absorption cross section ratio is used for O and Xe [62]

$$\frac{\sigma_{\text{Xe}}^{(2)}}{\sum_{J'} \sigma_{\text{O}, J \rightarrow J'}^{(2)}} = 1.9(\pm 20\%), \quad (6)$$

which takes into account all transitions into the upper excited states of atomic oxygen. In the measurements presented in this work, usually only the lowest $J = 2$ sub-level of the electronic ground state of O is probed. Particularly for measurements where humidity is added to the gas flow, the fluorescence signal from the other sub-levels is too weak to be detected reliably. In order to calculate the absolute density of all ground state sub-levels, the theoretical Boltzmann factor is applied

$$\frac{n_2}{n_0} = \frac{g_2}{\sum_{J=0,2} g_J \exp(-E_J/k_B T_g)}. \quad (7)$$

Here, n_2 is the density of the probed sub-level of the ground state, and n_0 is the density of the sum of all three ground levels. g is the statistical weighting, E_J the energy of the respective sub-level of the ground state, and T_g the gas temperature. The latter was measured with a thermocouple, about 315 K under our experimental conditions.

In *atomic hydrogen* the 3s and 3d sub-levels can be excited by the linearly polarised laser radiation at 205.08 nm according to the selection rules for two-photon absorption transitions,

but not the 3p sub-level. The spectral separation between the 3s and 3d states is about 0.15 cm^{-1} , so well within the laser bandwidth of about 4 cm^{-1} . The natural lifetimes of the 3s and 3d states are 159 ns and 15.6 ns, respectively [67, 68], while the theoretical ratio of the excitation cross sections $\frac{\sigma_d^{(2)}}{\sigma_s^{(2)}}$ is 7.56 [68]. Important for the TALIF calibration is that we use the natural lifetime $\tau_{\text{nat}} = 17.6 \text{ ns}$, as measured in [61], resulting from the weighted combination of the 3s and 3d states.

Krypton is the gas that is typically used to calibrate TALIF measurements of atomic hydrogen. Similar to the Xe-O calibration, the excitation wavelengths of Kr and H are spectrally close, as shown in figure 1. The fluorescence wavelengths differ by almost 200 nm, which results only in an insignificant change of the focal length of approximately $50 \mu\text{m}$ for the particular lens used in the ps-TALIF setup. The setup will be described in the next section.

For the two-photon excitation cross section ratio, the following value is used [61]

$$\frac{\sigma_{\text{Kr}}^{(2)}}{\sigma_{\text{H}}^{(2)}} = 0.62(\pm 50\%). \quad (8)$$

Similar to Xe, the cuvette is filled with Kr for the calibration measurement. The pressure in the calibration cell is chosen as 1 Torr. At higher pressures, there is the risk that amplified spontaneous emission disturbs the fluorescence characteristic and decay, as previously observed [69]. The purely optical branching ratio for the Kr transition of interest is $b = 0.953$ [70].

In the following paragraphs the measurement protocols for these quantities, as well as possible saturation effects, are discussed in detail.

2.2.2. Experimental apparatus. The modular laser set-up (EKSPLA) is shown in figure 2. It includes a Nd:YAG pump laser that incorporates a mode-locked oscillator together with regenerative and power amplifiers. The beam is directed into an amplification and harmonics generation unit, and subsequently enters an optical parametric generator and amplifier followed by sum-frequency and difference-frequency generation, which offers laser pulses of 30 ps duration at 10 Hz repetition rate with full spectral tunability between 193 and 2300 nm. The pulse energy in the UV range is a few hundreds of μJ within a spectral bandwidth of about 4 cm^{-1} . The laser pulse energy is varied with help of an attenuator-compensator system, which comprises two coated counter-rotating CaF_2 substrates that are controlled by a stepper motor. The standard deviation of the shot-to-shot fluctuations in the pulse energy is about 8%.

The laser beam is focused by a spherical plano-convex fused-silica lens with 30 cm focal length in a plane intentionally chosen about a centimetre behind the plasma effluent. This helps spreading the spatial laser pulse energy/power over a larger volume, resulting in a less stringent saturation level of the two-photon transition at the cost of a lower overall fluorescence signal, as well as staying below the material damage threshold of the calibration cuvette. The fluorescence radiation of the excited states is detected in the direction perpendicular

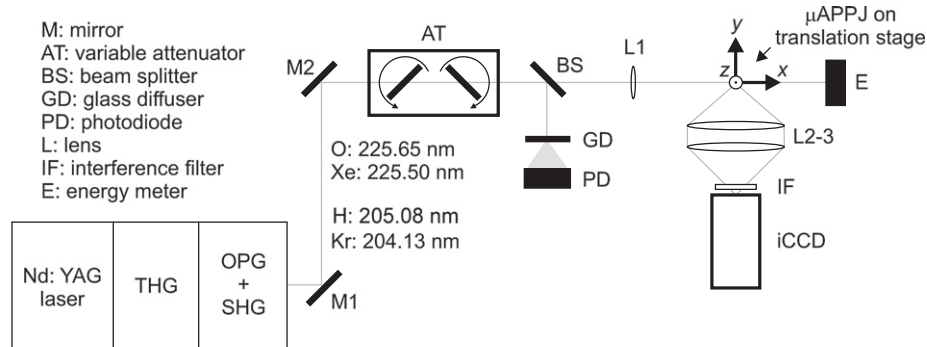


Figure 2. Schematic of the experimental setup depicting the picosecond laser system and the components used for beam energy control and fluorescence detection. The APPJ is mounted on a translation stage for spatial mapping of the effluent in the y - z plane.

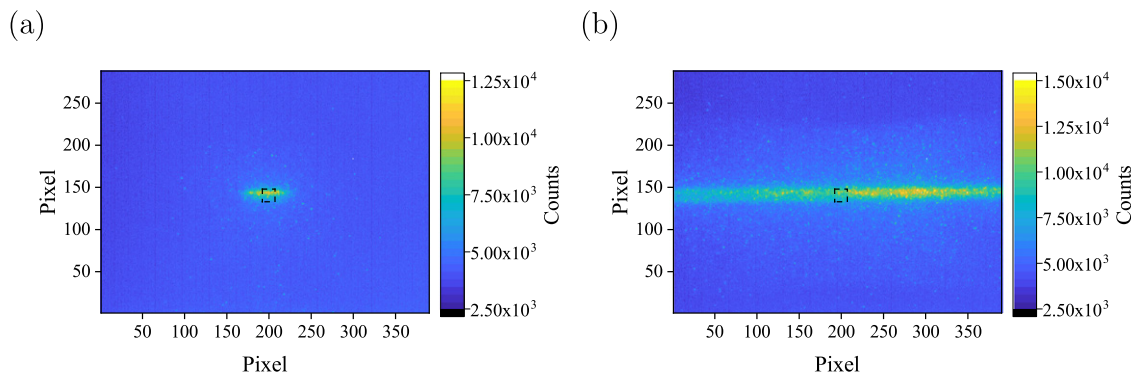


Figure 3. Example of fluorescence images taken with the ICCD camera: (a) for atomic oxygen, (b) for xenon. The dashed black rectangle indicates the ROI.

to the laser beam using an intensified charge coupled device camera (iCCD: Stanford Computer Optics 4-Picos, 780×580 array, $8.3 \mu\text{m}^2$ pixels, S25IR photo-cathode) subsequent to its passage through a doublet of achromatic lenses (diameter 50 mm, focal length 80 mm each) and an interference filter (central wavelengths $\lambda_{\text{O}} = 845$ nm, $\lambda_{\text{H}} = 656$ nm, $\lambda_{\text{Xe}} = 835$ nm, $\lambda_{\text{Kr}} = 825$ nm, each with a full-width-at-half-maximum of 10 nm).

2.2.3. Signal measurement. As already mentioned, S is the spatially, temporally, and spectrally integrated fluorescence signal. The spatial integration is performed by choosing a defined region of interest (ROI) from the camera image, in which the signal is summed up. This means that the spatial resolution is limited by the choice of ROI. Typically, images are obtained by the accumulation of light from 64 or 128 individual laser shots, with the accumulation being carried out on the camera chip. Figure 3(a) shows the fluorescence signal of O^* at 844 nm, at the strongest excitation wavelength of 225.65 nm. A bright region is visible approximately in the middle of the camera image where the laser beam intersects with the jet effluent region, leading to excitation of O from the ground state, and subsequent emission of fluorescence. Similarly, figure 3(b) shows the fluorescence signal obtained from the calibration with Xe at 835 nm and a laser wavelength of 224.30 nm. The calibration cuvette containing the Xe gas has much larger dimensions compared to the 1 mm discharge gap of the μAPPJ , therefore, the fluorescence signal is visible

over the whole width of the CCD chip. For both measurements, the same ROI is chosen, as indicated in the figures.

The temporal integration is performed by choosing the camera gate width long enough to collect almost all of the exponential fluorescence decay after the laser pulse ($>98\%$ under all measurement conditions). Among the four species of interest, we measured the longest effective lifetime of 21.4 ns for $\text{Kr}(5p'[3/2]_2)$ at 1 Torr in the cuvette. Therefore, a camera gate width of 100 ns is chosen, which means that 98%–99% of the fluorescence signal is captured, depending on the camera start delay. The same gate width is chosen for all other species, leading to a light capture higher than 99.9%.

Temporal and spatial integration of the fluorescence signal yields the spectrally dependent fluorescence signal $s(\lambda)$, which is a function of laser wavelength over the resonant transition. The minimum wavelength step of the laser is 0.01 nm when tuned. With this spectral resolution we measure at 9 different laser wavelengths around the absorption line. Additionally, a measurement of the background signal is performed by manually closing the shutter of the laser output. By subtracting this background signal, potential background light, optical plasma emission, and the base noise of the detector is accounted for. Scattered laser stray light is no issue, since all the detection optics are not UV transparent. Spectral integration of $s(\lambda)$ results in the absolute fluorescence signal S_{F} . Typical wavelength scans for atomic hydrogen and oxygen are shown in figure 4.

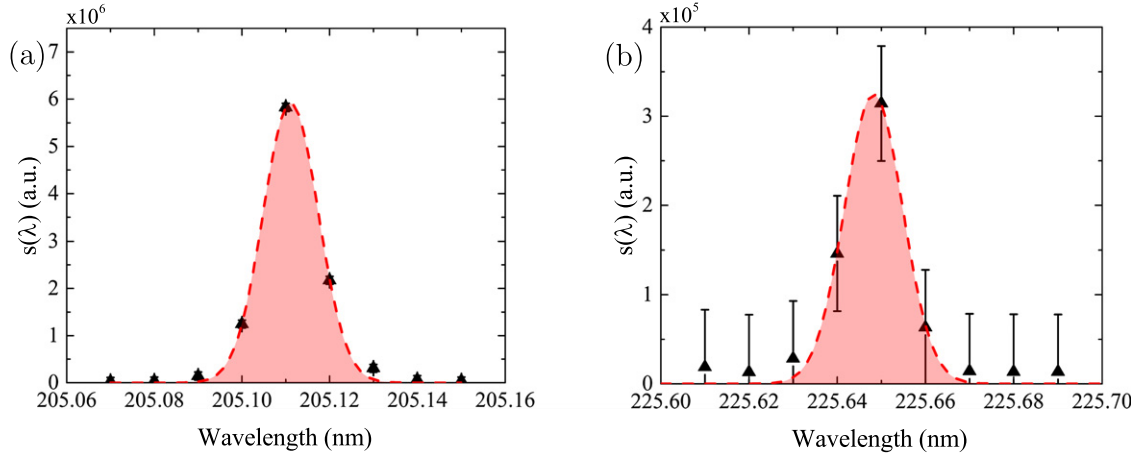


Figure 4. Normalised fluorescence signal for (a) H^* and (b) O^* 500 sccm He with a H_2O content of 1240 ppm, 510 V_{pp} . Error bars show the standard deviation of the noise. The data is fitted with a Gaussian function.

The overall fluorescence signal is determined as the area of a Gaussian function that is fitted to the measured line profile $s(\lambda)$. The overall line profile is dominated by the laser line profile, whose bandwidth as stated by the manufacturer is about 4 cm^{-1} ($\Delta\lambda = 20 \text{ pm}$). This is less than ten times the theoretical Fourier limit, when considering the pulse duration of 32 ps. The other broadening mechanisms, i.e. Doppler and pressure broadening, are about an order of magnitude smaller under our experimental conditions.

For atomic oxygen, the Doppler broadening $\Delta\lambda_D$ can be calculated as

$$\Delta\lambda_D^O = \frac{\lambda}{c} \sqrt{\frac{8k_B T_g \ln(2)}{m_O}} = 0.35 \text{ pm}, \quad (9)$$

where $T_g = 315 \text{ K}$ and $\lambda = 112.8 \text{ nm}$ as half the excitation wavelength for atomic oxygen, which is in good agreement with measured values [71]. For atomic hydrogen, $\Delta\lambda_D^H = 1.3 \text{ pm}$, which is still more than a factor 10 smaller than the laser bandwidth.

Pressure broadening coefficients for O by He and O_2 were determined in reference [71]. For 1 bar, pressure broadening by the background He can be calculated as

$$\Delta\lambda_L^O = 0.59 \text{ pm}, \quad (10)$$

assuming that pressure broadening is dominated by the He background gas.

In general, our pico-second laser system offers a balanced compromise between temporal and spectral resolution when compared to typical nano-second and femto-second UV TALIF laser systems [54].

The quality of the signal measurement strongly depends on the investigated species and the experimental circumstances, and the signal-to noise ratio, which is defined here as

$$\text{SNR} = \frac{s - s_0}{\Delta\text{noise}}, \quad (11)$$

where Δnoise is the standard deviation of the measured noise, and $s_{\text{net}} = s - s_0$ the net mean fluorescence signal, which means the signal averaged over the ROI, s , minus the average

background s_0 . For example, when measuring atomic hydrogen under a H_2O variation, the measured H fluorescence signal is strong since H densities produced from H_2O are high. Figure 4(a) shows normalised fluorescence signal of H^* as a function of the laser wavelength. The SNR for this measurement is good, resulting in a small Δnoise (shown as error bars) compared to the signal strength. On the contrary, for a measurement of O under a H_2O admixture, the signal to noise ratio is small, because the O densities produced from H_2O are low. This is shown in figure 4(b).

As discussed previously, the laser steps are limited to 0.01 nm, resulting in typically 4–5 possible measurements where a signal is obtained for each wavelength scan. Although a Gaussian function can usually be fitted to the experimental data with no difficulties, the fact that so few points are available for the fit makes it difficult to assess the accuracy of the fitting procedure, particularly when the SNR is low. Estimates of the related uncertainty are given in section 2.2.6.

2.2.4. Lifetime measurement. In order to measure τ_{eff} in equation (5) with the ps-TALIF setup, the gate width of the camera is fixed, and the camera delay is increased incrementally, so that the fluorescence signal $s(\lambda)$ at different times after the laser pulse is obtained.

Typical camera gate steps are chosen as 0.5 ns for O^* , 0.2 ns for H^* , 1 ns for $\text{Xe}(6p'[3/2]_2)$, and 2 ns for $\text{Kr}(5p'[3/2]_2)$. Typical gate widths are chosen as 10 ns for O^* , 2 ns for H^* and $\text{Xe}(6p'[3/2]_2)$, and 10 ns for $\text{Kr}(5p'[3/2]_2)$, respectively. Since the camera gate widths are larger than the respective gate steps, the measured signals overlap temporally. Particularly the long gate widths for the lifetime measurements of O^* and $\text{Kr}(5p'[3/2]_2)$ have been chosen due to the low signal-to-noise ratio for these measurements. It was tested before for the same plasma operating conditions, that the choice of gate step (between 0.2 and 1 ns) and width (between 2 and 20 ns) does not have an effect on the measured lifetimes (see figure 5).

As for the signal measurements, the quality of the lifetime measurement strongly depends on the investigated species and the experimental circumstances, and the signal-to-noise ratio. The lifetime of the excited species can be obtained by fitting

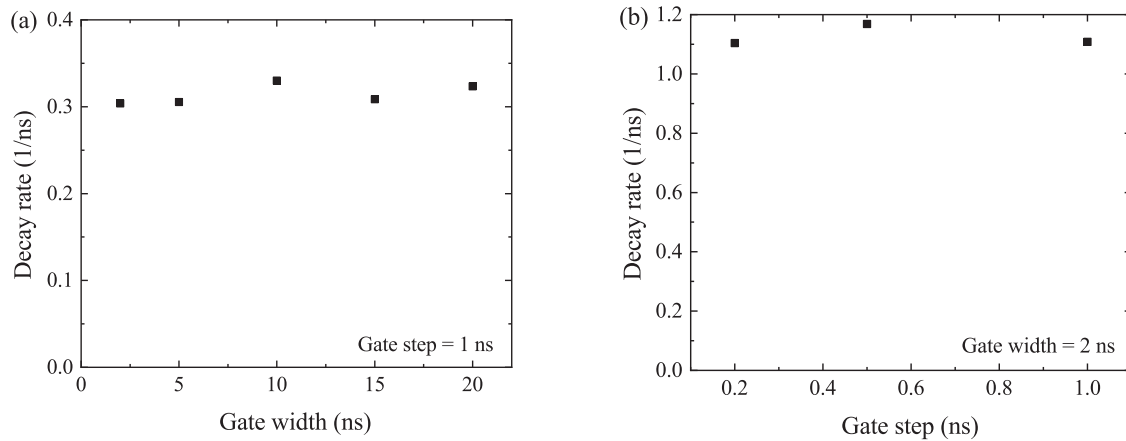


Figure 5. Measured decay rates of (a) O* as a function of gate width at constant gate step (0.5 slm He, 4130 ppm H₂O) and (b) H* as a function of gate step at a constant gate width (1 slm He, 1040 ppm H₂O).

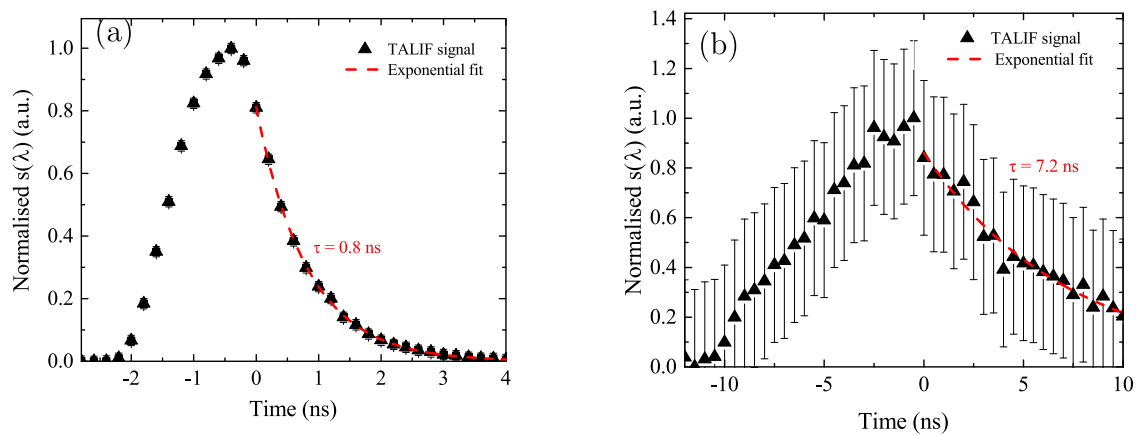


Figure 6. Normalised measured fluorescence decay for (a) H* and (b) O* at 500 sccm He, H₂O content of 1240 ppm, 510 V_{pp}. Error bars show the standard deviation of the noise.

an exponential decay to the measured TALIF signal. This is shown in figure 6 for measurements of the atomic hydrogen and oxygen fluorescence for the same plasma conditions. Similar to the previous discussion, atomic hydrogen is produced in large quantities from H₂O (figure 6(a)), resulting in a good signal-to-noise ratio, whereas O densities produced from H₂O are much smaller (figure 6(b)), and Δnoise is large compared to the fluorescence signal. However, a large number of points is generally taken, and the fluctuation of the measurement is small. The decay can be easily fitted by an exponential decay, with stated error bars according to a 95% confidence band. The effective lifetimes for Xe(6p'[3/2]₂) and Kr(5p'[3/2]₂) (at 10 Torr and 1 Torr pressure) have been measured each time an absolute calibration was performed. The lifetimes and their uncertainties are therefore calculated as the average and standard deviations from multiple measurements as $\tau_{\text{eff}}^{\text{Xe}(6p'[3/2]_2)} = 6.5 \pm 0.5$ ns and $\tau_{\text{eff}}^{\text{Kr}(5p'[3/2]_2)} = 21.4 \pm 0.8$ ns, respectively.

2.2.5. Choice of laser energy. The calibration according to equation (3) only holds when the observed TALIF signal depends on the square of the laser pulse energy. This is the case

for weak enough laser energy to only excite a small amount of the ground state atoms, and not disturb the system otherwise. In reality, several effects can occur, if the laser energy is chosen to be too high, such as photo-dissociation of molecules being present in the gas, or photo-ionisation when a third photon is absorbed by the already excited atom. These effects would lead to a deviation of the square dependence of the TALIF signal and the laser pulse energy. This can be easily checked by varying the laser pulse energy, and plotting the spectrally integrated TALIF signal S_F against the squared laser pulse energy.

In this work, we can observe saturation effects at higher laser pulse energies for O, Xe, and Kr, while for H no saturation was observed for energies up to 40 μJ. For all measured species, we choose laser pulse energies that are well below the saturation limit, respectively: 24 μJ (O), 35 μJ (H), 0.45 μJ (Xe), and 0.28 μJ (Kr). The pulse energies for the probing species (O and H) are much lower compared to ns-TALIF setups, where typical laser energies lie in the range of millijoules [40, 62]. Therefore, comparing the ps-TALIF setup with a standard ns-TALIF setup, average powers are lower for the ps-TALIF setup. Pulse peak powers of the two systems are about in the same order of magnitude ($\sim 10^5$ W).

Table 1. Constants used for calculation of absolute densities according to equation (3) for the excitation wavelength λ_L , the natural lifetime τ_{nat} , the purely optical branching ratio b , the laser energy E_L , the quantum efficiency η , and transmissions of several optics. T_f , T_c^L and T_c^F are the transmission of the optical filter, and the single-wall transmission of the calibration cuvette for the laser and fluorescence signals, respectively.

Species	λ_L (nm)	τ_{nat} (ns)	b	E_L (μJ)	T_f (%)	T_c^L (%)	T_c^F (%)	η (%)
O	225.65	34.7	1	24	83.7	—	—	9.10
H	205.11	17.6	1	35	88.9	—	—	13.23
Xe	224.31	40.8	0.733	0.45	62.9	92	94	9.65
Kr	204.13	34.1	0.953	0.28	73.7	90	94	10.35

2.2.6. Constants and error estimation. Table 1 shows values used together with equation (3) to calculate absolute densities of O and H. Values for the natural lifetimes as well as branching ratios have been taken from references [61, 62]. As discussed previously, the laser energy is usually monitored using an energy meter. Values for the quantum efficiency of the detector were taken as stated by the manufacturer. The spectral transmission of the optical filters were previously measured using a Shimadzu UV-1800 UV-VIS spectrophotometer with 0.1 nm resolution [69]. The transmission of the calibration cuvette was determined by measuring the laser pulse energy in front and behind the cuvette.

Table 2 lists the estimated standard deviations of the individual quantities relevant for the TALIF calibration as well as the overall uncertainty for the absolute atomic density results. The uncertainties of the cross section ratios and natural lifetimes are taken from references [61, 62]. The uncertainty of τ_{eff} for the calibration gases is calculated as the standard deviation of several independent measurements, as discussed previously. The uncertainties related to the signal measurements are estimated based on the uncertainty in the area under the curve of the fluorescence signal determined from the fitting procedure. The uncertainty for the measurement of the signal for O is larger than that for H, in part due to the low value of the signal with respect to the standard deviation of the noise, which influences the accuracy of the background subtraction.

The resulting uncertainties for the calculation of absolute species densities under several experimental conditions are calculated from the various error bars in table 2. The highest error of 58% is associated with the measurement of H in H_2O containing plasmas due to the high uncertainty of the two-photon excitation cross section ratio.

3. Global model

Measured absolute densities of O and H are compared with a 0D plasma-chemical kinetics model [72] using the GlobalKin code [73]. The considered species and list of reactions are identical to those presented in [57].

The plasma is simulated by assuming a cross section of $(0.1 \times 0.1) \text{ cm}^2$ and 3 cm channel length. Simulations are carried out as described in [57]. The input power is set to 0.3 W, which is in good agreement with [56], and the gas temperature is self-consistently calculated using the GlobalKin code. Simulations are run using a pseudo 1D plug flow and

Table 2. Estimated relative uncertainties (in %) for several quantities in equation (3), as well as the resulting overall relative uncertainties for absolute densities measured under different conditions, which are O densities under an admixture of O_2 and H_2O , as well as H densities under an admixture of H_2O .

	T_c	E_L	$\frac{\sigma_{\text{cal}}^{(2)}}{\sigma_{\text{x}}^{(2)}}$	τ_{nat}	τ_{eff}	S_F	n
Species	O	8		5		—	
	H	8		10		—	
	Xe	3	8	5	7	10	
	Kr	3	8	10	4	10	
Measurement	O- H_2O		20		11	15	39
	H- H_2O		50		5	5	58

a He gas flow of 500 sccm, resulting in gas velocities around 960 cm s^{-1} . For some investigations, simulations are extended into the plasma effluent, where the power is set to zero. In addition, water vapour up to 5000 ppm (0.5%) is admixed. For some simulations, O_2 impurities up to 12 ppm are assumed in the initial gas mixture, corresponding to an air impurity of 60 ppm, in order to investigate the potential effect of gas impurities, i.e. up to 32 ppm air in the used gas bottle of helium, as stated by the supplier, or by reflux from the ambient air into the discharge channel. We do not take into account any nitrogen species in the simulations, however, since we mainly investigate the formation of oxygen and hydrogen containing species in this work, we assume that nitrogen species are not directly involved in their formation mechanisms.

4. Determination of quenching with H_2O

The sub-nanosecond temporal resolution of the experimental diagnostic setup enables the measurement of effective decay rates (natural decay rate and influence of collisional quenching) at atmospheric pressure. This allows for the determination of quenching coefficients for the laser-excited states with several quenching molecules, in this case H_2O . For this, effective decay rates are measured approximately 1 mm from the nozzle of the plasma jet as a function of H_2O density in the feed gas, which is shown in figure 7 for O^* and H^* . The widening of the error bars for the O^* decay rate with increasing H_2O admixture reflects the decrease of the TALIF signal towards the detection limit.

If the decay rates are linearly dependent on the H_2O content, quenching coefficients can be calculated from the slopes

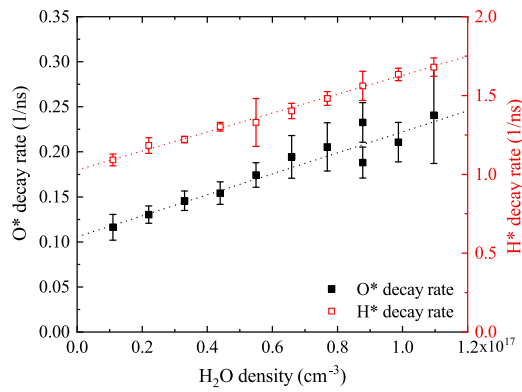


Figure 7. Measured decay frequencies of O^* and H^* as a function of H_2O content in the feed gas. Measurements were taken at 500 sccm total gas flow, and 510 V_{pp}. Error bars show uncertainties from the exponential decay fitting to the raw data.

of the linear fits. Table 3 shows a comparison of quenching coefficients obtained in this work with literature values. They will be discussed in more detail in the next sections.

The calculation of the quenching coefficients from the slopes of the linear fits in figure 7 is based on several assumptions: (a) The main quenching partners are He and H_2O according to the feed gas composition at a gas pressure of 1 atm and a gas temperature of 315 K near the plasma nozzle, as measure with a thermocouple. (b) The small decrease in He density with increasing H_2O density at constant gas flux was neglected, since the resulting relative error, given by k_{He}/k_{H_2O} , for the derived quenching coefficients turned out to be insignificant (less than one percent in our case). (c) The intrinsic dependence $k \propto \langle v \rangle \propto T_g^{1/2}$ of the quenching coefficients via the mean collision velocity $\langle v \rangle$ on the gas temperature T_g (in Kelvin) is neglected. For *non room temperature* applications, the stated quenching coefficients need to be scaled accordingly. (d) The major simplification is to disregard the fraction of H_2O molecules dissociated along the discharge channel, given as

$$D_{H_2O} = \frac{n_{H_2O}(0 \text{ cm}) - n_{H_2O}(3 \text{ cm})}{n_{H_2O}(0 \text{ cm})} \times 100. \quad (12)$$

In the simulations operated at $P = 0.3$ W, and very low H_2O content in the feed gas (1 ppm), up to 33% of the admixed H_2O molecules are dissociated in the plasma by the time they reach the end of the plasma channel. The dissociation fraction rapidly decreases with increasing H_2O admixture. For admixtures greater than 500 ppm, the dissociation degree settles to a value of about 3.8%, and provides an additional uncertainty to the values in table 3.

A fluctuation of the bubbler temperature within the error bar of 1°C leads to an uncertainty of 6%, in addition to the uncertainties in table 3. The bubbler is not temperature controlled for these measurements.

4.1. Quenching of $O(3p^3P)$ with H_2O

The quenching coefficient $k_{H_2O}^{O^*} = 1.1 \times 10^{-9} \text{ cm}^3 \text{ s}^{-1}$ is obtained from the slope of measured decay rates shown in

figure 7 (black squares and dashed black line) with an uncertainty of 10% from the linear fit.

A literature value for the room temperature quenching coefficient of O^* with H_2O has been obtained previously by Quickenden *et al* [74] as $k_{H_2O}^{O^*} = (9.4 \pm 1.5) \times 10^{-10} \text{ cm}^3 \text{ s}^{-1}$ using radiolysis of pure water vapour with an electron beam, and detection of fluorescence light using a photo-multiplier. The water vapour was created by heating up a supply of water connected to their experimentation cell. Meier *et al* [75] have measured the same room temperature quenching coefficient using TALIF in a flow-tube reactor as $k_{H_2O}^{O^*} = (4.9 \pm 0.3) \times 10^{-9} \text{ cm}^3 \text{ s}^{-1}$ under low pressure conditions in the mbar range. The literature values for quenching coefficients for O^* with H_2O do not agree well with each other. The O^* quenching coefficient with H_2O obtained in this work lies between the two available literature values, but closer to the quenching coefficient measured by Quickenden *et al* [74], although this is the older of the two cited sources, and a non-linearity between quenching rates and H_2O content was observed in their experiment.

By extrapolating the linear fit to zero H_2O admixture in figure 7, a lifetime of $\tau_{O^*,\text{eff}} = 9.6 \text{ ns}$ is obtained for pure He. Taking the natural lifetime of O^* $\tau_{O^*,\text{nat}} = 34.7 \text{ ns}$ [62], a quenching coefficient for O^* with He can be determined as $k_{He}^{O^*} = 0.032 \times 10^{-10} \text{ cm}^3 \text{ s}^{-1}$ using

$$k_{He}^{O^*} = \frac{\frac{1}{\tau_{O^*,\text{eff}}} - \frac{1}{\tau_{O^*,\text{nat}}}}{n_{He}}. \quad (13)$$

This value lies within the broad span of the literature values ranging from 0.016 to $0.15 \times 10^{-10} \text{ cm}^3 \text{ s}^{-1}$ for the room temperature quenching coefficient [53, 61, 62, 76].

4.2. Quenching of $H(n=3)$ with H_2O

The quenching coefficient $k_{H_2O}^{H^*} = 6.0 \times 10^{-9} \text{ cm}^3 \text{ s}^{-1}$ is obtained from figure 7 (red open squares) with an uncertainty of 3% from the linear fit. The measured values are significantly smaller than the literature values $k_{H_2O}^{H^*} = (9.1 \pm 1.6) \times 10^{-9} \text{ cm}^3 \text{ s}^{-1}$ and $k_{H_2O}^{H^*} = (1.1 \pm 0.1) \times 10^{-8} \text{ cm}^3 \text{ s}^{-1}$ from [74, 75] for the room temperature quenching coefficient, respectively, although obtained by the same techniques as described in section 4.1.

From the intercept of linear fit in figure 7, an effective lifetime $\tau_{H^*,\text{eff}} = 1.0 \text{ ns}$ is obtained in pure He. Using the literature value $\tau_{H^*,\text{nat}} = 17.6 \text{ ns}$ [53, 61, 68] for the natural lifetime of H^* and equation (13), we derive the quenching coefficient $k_{He}^{H^*} = 0.42 \times 10^{-10} \text{ cm}^3 \text{ s}^{-1}$. This value is close to the most recently determined literature value $k_{He}^{H^*} = 0.317 \times 10^{-10} \text{ cm}^3 \text{ s}^{-1}$ [53] for the room temperature quenching coefficient, while older literature values range from 0.099 to $0.53 \times 10^{-10} \text{ cm}^3 \text{ s}^{-1}$ [61, 68, 76].

5. Atomic species as a function of humidity

5.1. Atomic oxygen

Figure 8(a) shows the O densities measured under a variation of humidity in the feed gas approximately 1 mm from the

Table 3. Measured quenching coefficients for O* and H* with H₂O and comparison with literature values.

Species	Quenching species	k_q (cm ³ s ⁻¹)	k_q^{lit} (cm ³ s ⁻¹)	Reference
O(3p ³ P)	H ₂ O	1.1×10^{-9} ($\pm 10\%$)	$(9.4 \pm 1.5) \times 10^{-10}$	[74]
			$(4.9 \pm 0.3) \times 10^{-9}$	[75]
H($n = 3$)	H ₂ O	6.0×10^{-9} ($\pm 3\%$)	$(9.1 \pm 1.6) \times 10^{-9}$	[74]
			$(1.1 \pm 0.1) \times 10^{-8}$	[75]

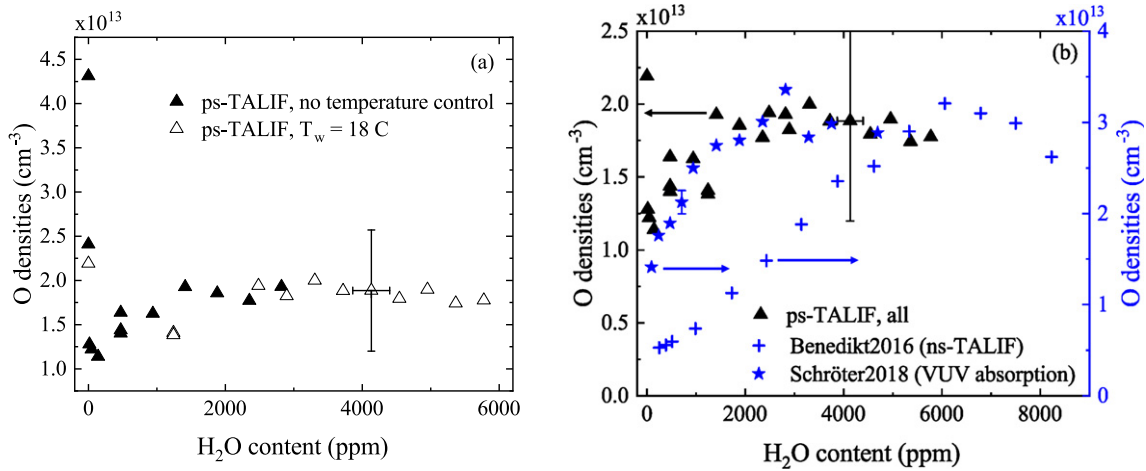


Figure 8. Absolute ground state atomic oxygen densities as a function of humidity content of the He feed gas (black triangles). Measurements were taken at 500 sccm total gas flow, and 510 V_{pp}. (a) ps-TALIF measurements. (b) Zoom into ps-TALIF results, ignoring high density values at low H₂O admixtures. Data shown in blue is a comparison with literature values. Stars: Schröter *et al* [57]; crosses: Benedikt *et al* [60].

nozzle of the plasma jet. Above 100 ppm, the O density increases slightly with increasing humidity admixture, until it reaches a maximum level of about 2×10^{13} cm⁻³ at around 2000–2500 ppm. At very low H₂O content, however, a sharp increase of O density with decreasing H₂O content is observed, which is shown in figure 8(a). A peak value of 4.3×10^{13} cm⁻³ is obtained before H₂O is actively admixed to the He background gas. Interestingly, this high value cannot be reproduced when this data point is retaken after admixing H₂O to the feed gas. This is a strong indicator that residual H₂O from previous measurements attached to the feed gas line is still present, which changes the plasma chemistry, compared to a measurement that was started with a dry feed gas line. Therefore, the points measured at low *intentional* H₂O admixtures are believed to be very dependent on feed gas impurities, as discussed further below.

The observed trend agrees very well with previously investigated O densities measured by vacuum ultra-violet Fourier-transform absorption spectroscopy (VUV-FTAS) [57], which are shown in figure 8(b) as blue stars. However, maximum O densities measured with ps-TALIF in the μ APPJ are about 70% of the O densities measured with VUV-FTAS in previous investigations. Possible reasons for this difference could lie in the different surface-to-volume ratios of the two sources, resulting in different recombination probabilities for species such as H at the reactor walls [77], leading to a changed chemistry in the plasma bulk, and the fact that O is measured at different positions in the jet using the two setups (in the

centre of the discharge at 1.2 cm in [57] and outside the channel in this work). Differences in measured absolute densities can also arise from the two very different diagnostic techniques used here and in the previous investigations (ps-TALIF vs. VUV-FTAS) and the uncertainties associated with them.

A comparison with the data of Benedikt *et al* [60], also shown in figure 8(b) as blue crosses, demonstrates good quantitative agreement within a factor 1.5–2.5, depending on H₂O content. Their measurements have been carried out using ns-TALIF in a controlled He atmosphere. Under their plasma operating conditions (1.4 slm total He flow, 565 V_{pp}), they observed an increase in O density up to 3×10^{13} cm⁻³ at 6000 ppm, followed by a short decrease until the plasma extinguished at 8000 ppm. Therefore, their measured O peak densities are about a factor 1.5 larger than the values obtained in this work. One possible reason for the difference lies in the fact that with their ns-TALIF system, Benedikt *et al* were not able to determine their O* lifetimes experimentally. Instead, they calculated the effective decay rate using the quenching coefficient $k_{\text{H}_2\text{O}}^{\text{O}^*} = 4.9 \times 10^{-9}$ cm³ s⁻¹ from reference [75], which is much larger than the coefficient $k_{\text{H}_2\text{O}}^{\text{O}^*} = 1.3 \times 10^{-9}$ cm³ s⁻¹ obtained in this work. Since the absolute O densities depend linearly on A_{eff} , as shown in equation (5), and therefore on the quenching coefficient, the use of a larger quenching coefficient would lead to higher densities, and potentially also different trends in O densities, as observed in figure 8. In addition, our

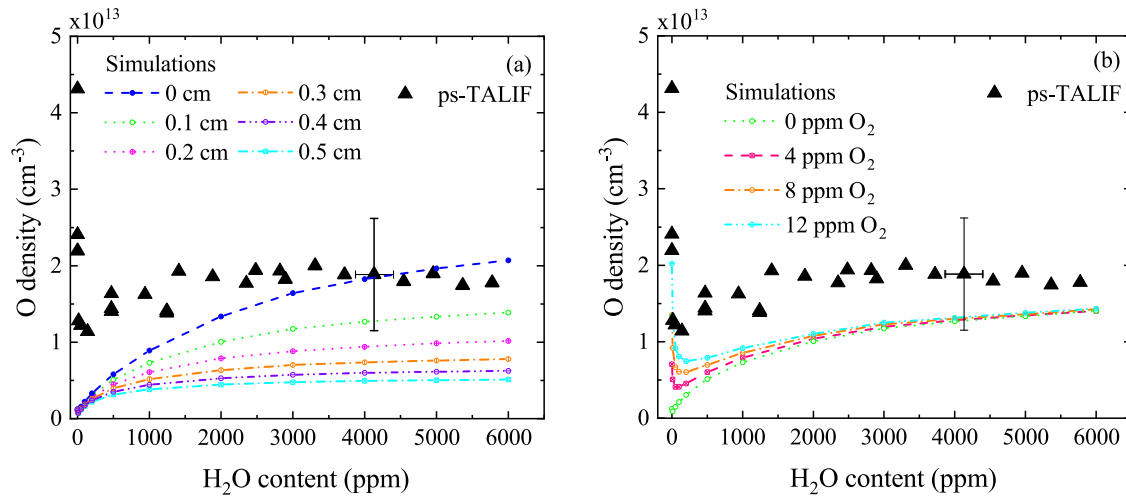


Figure 9. Measured absolute O densities under a variation of the humidity content (triangles), as in figure 8. (a) Simulation results for absolute O densities as a function of H₂O content and distance from the plasma nozzle, for a plasma power of 0.3 W. (b) O densities as a function of H₂O for different air impurity contents, for a plasma power of 0.3 W and distance 0.1 cm from the nozzle.

experimental investigations were carried out under slightly different plasma conditions (510 V_{pp}, 0.5 slm He flow) compared to the investigations by Benedikt *et al* (565 V_{pp}, 1.4 slm He flow), which could also affect both observed trends and absolute densities. Particularly the higher applied voltage in the work of Benedikt *et al* could lead to a shift of maximum O densities towards higher water contents.

Additionally, using ps-TALIF, a strong increase of O towards very low admixtures is observed in this work, which can be seen best in figure 8(a). These high O densities at low admixtures are most likely due to impurities in the feed gas, either because of O₂ entering the feed gas through small leaks, diffusion of O₂ from the ambient air, impurities from the gas line, or impurities present in the gas bottle. The fact that we did not observe these high O densities at low admixtures in earlier work using VUV-FTAS [57], where measurements were carried out in a closed source with no contact to ambient air, supports a potential role of small leaks or diffusion from the ambient air. In addition, Benedikt *et al* [60] also do not observe these high densities at low admixtures, potentially because their measurements were carried out in a He atmosphere. In addition, we assume that this effect would be less observable at higher flow rates as used by Benedikt *et al*, because ambient air is less likely to enter the gas flow. However, it is also important to note that the measurements of O carried out in [57, 60] used 5.0 grade He, compared with the 4.6 grade He used in this work. As such, a contribution of higher gas bottle impurities in this work cannot be completely excluded.

In order to investigate the influence of impurities and distance to the plasma nozzle further, GlobalKin simulations are carried out for the μ APPJ. Figure 9 shows simulated absolute atomic oxygen densities together with the measurement results for a variation of the humidity content in the feed gas.

The dashed lines in figure 9(a) indicate the absolute simulated O densities as a function of H₂O content in the feed gas, for different distances from the nozzle, and without any air impurities. The O density decreases with increasing distance

to the nozzle, due to consumption of O in chemical reactions, mainly with OH



Consumption by reactions with HO₂ gain more importance further away from the nozzle



The trends for O densities under a humidity variation depend on the distance from the jet nozzle. While directly at the nozzle at 0 cm [blue line in figure 9(a)], O densities are monotonically increasing with increasing H₂O admixture, O densities a few millimetres away from the nozzle approach a steady-state value at high H₂O admixtures. ps-TALIF measurements were carried out at approximately 1 mm distance to the plasma nozzle [green line in figure 9(a)]. At this distance, trends in the simulation and experiments are slightly different at high H₂O content. In the simulation, O densities clearly increase with increasing H₂O admixture. In the experiment, a plateau is reached at about 1500 ppm. At higher admixtures, O densities stay constant within the error bars of the measurement. The tendency of the simulated O density to increase at H₂O admixtures above which the measured density appears to saturate may be explained by a range of factors. For example, the simulations may underestimate the rate of electron energy loss with increasing H₂O admixture, leading to an overestimation of ionisation and dissociation rates at higher H₂O admixtures. A similar effect was observed and discussed in [57] when comparing measured and simulated OH densities under similar conditions. In general, the saturation, or decrease in the concentration of radicals with increasing molecular gas content is well established for atmospheric pressure plasma sources, as discussed in [2, 40, 47, 60], for example. Aside from this, simulated and measured absolute O densities agree within about a factor of 2, which is considered to be good agreement, particularly considering that the formation of O from H₂O is

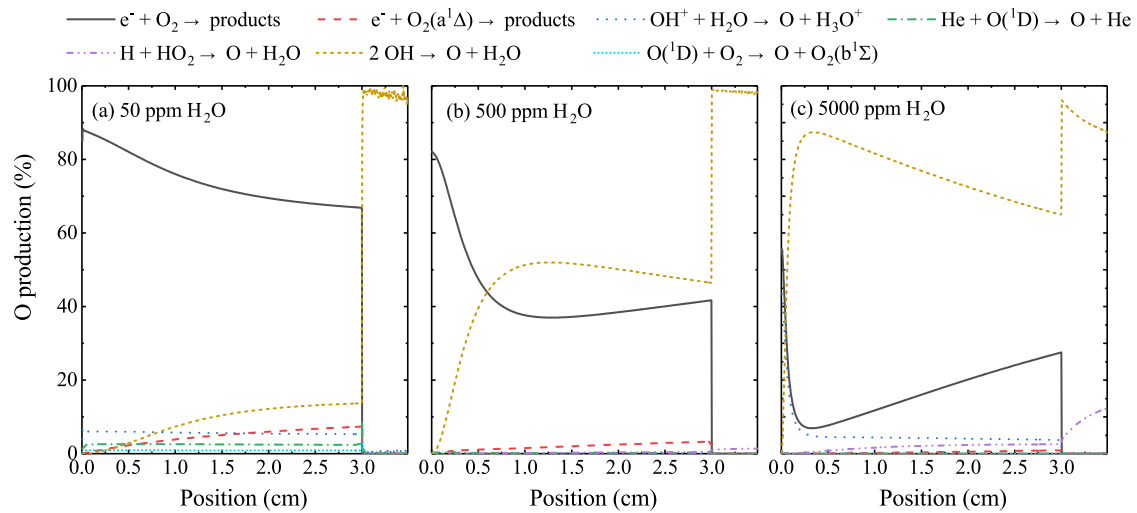


Figure 10. Formation pathways for O at different humidity contents for a fixed O_2 admixture of 8 ppm, 0.3 W and 500 sccm total He flow.

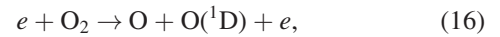
complex, in the sense that it is not primarily produced from direct dissociation of H_2O molecules.

In order to investigate the role of impurities in the feed gas flow, different O_2 impurity concentrations of 4, 8, and 12 ppm are assumed in the initial gas mixture. As a comparison, the amount of air impurity in a He 4.6 grade bottle is 32 ppm according to the gas supplier, corresponding to an O_2 impurity of ≈ 6 ppm. The absolute O densities simulated under these conditions are shown in figure 9(b) for a distance of 1 mm from the nozzle. In the simulation, at very low H_2O admixtures, <100 ppm, O densities sharply increase towards decreasing H_2O admixtures, as observed in the experiments. These simulations support the hypothesis that the increase in O density at low H_2O content is due to the presence of O_2 impurities in the feed gas, and allow an estimation of the concentration required to explain the experimental observations i.e. ≈ 10 ppm. This concentration is in the same order of magnitude as that contained in the gas bottles used in this work, but does not exclude a potential role for other sources of impurities, such as adsorbed O_2 in the gas lines, leaks or diffusion from the ambient air. At high humidity admixtures, the addition of air impurities only makes a small difference to absolute O densities. It is therefore concluded that plasmas can be operated in a more controlled way by purposefully admixing molecules into the feed gas, because the produced reactive species are not as strongly influenced by ambient conditions, which are susceptible to change unless the plasma is operated in a shielding gas atmosphere.

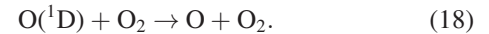
The very good agreement between simulations and experiments means that the production and consumption reactions for different H_2O admixtures can be investigated. In the following discussion, a pathway analysis is carried out for an O_2 impurity content of 8 ppm because this value is closest to the intrinsic oxygen impurity level of the used He feed gas. An overview of the different pathways can be found in figures 10 and 11.

The production pathways for O at different H_2O contents are shown in figure 10. At a H_2O admixture of only

50 ppm, the plasma chemistry is mainly dominated by the oxygen reactions originating from oxygen impurities. O is mainly produced by electron impact dissociation of molecular oxygen



and the equivalent processes from the $O_2(a^1\Delta)$ and $O_2(b^1\Sigma)$ states. Further O is produced via quenching of excited $O(^1D)$



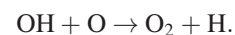
Equations (16)–(18) have been previously identified as being the main production channels for O in He- O_2 APPs in a similar plasma source [78].

As the H_2O content increases, these processes become less relevant, and are increasingly replaced by reactions including hydrogen containing species. Particularly



which was found to be important for the formation of O in [57] and is found to play a key role in the formation of O under these conditions as well. This reaction becomes the dominant production mechanism at high H_2O admixtures. Dissociation of O_2 remains one of the dominant production mechanisms also at high H_2O admixtures, since O_2 is actively formed in H_2O containing plasma, as discussed in [57]. On the other hand, densities of $O(^1D)$ decrease rapidly with increasing admixture of water, therefore, quenching of $O(^1D)$ becomes less important for the production of O at higher H_2O contents.

The O consumption pathways are shown in figure 11. For 50 ppm H_2O , the first few mm in the plasma are dominated by losses to the wall. After that, and for all positions for higher H_2O content, the main consumption pathway is equation (14),



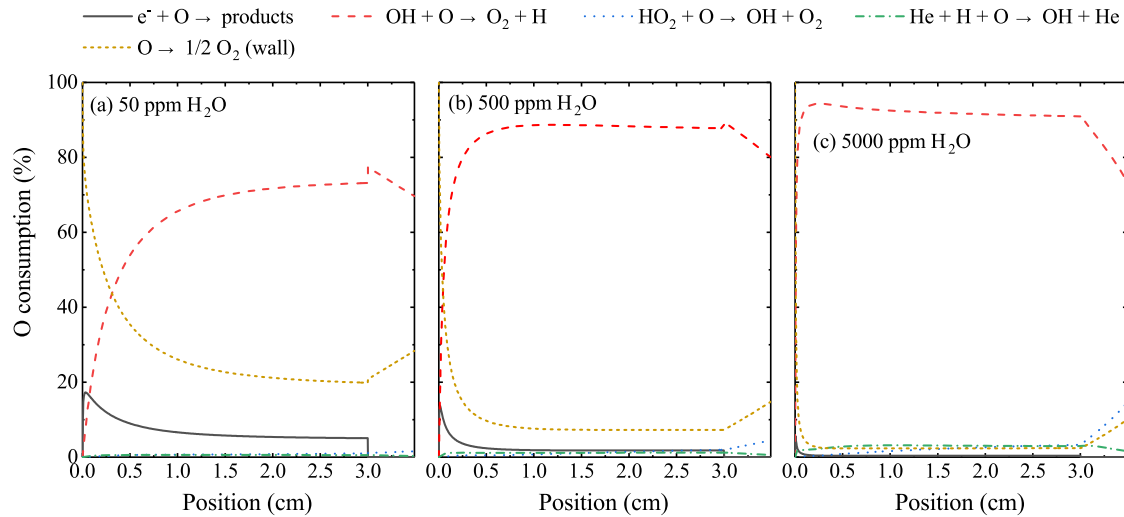


Figure 11. Consumption pathways for O at different humidity contents and a fixed O₂ admixture of 8 ppm, 0.3 W and 500 sccm total He flow.

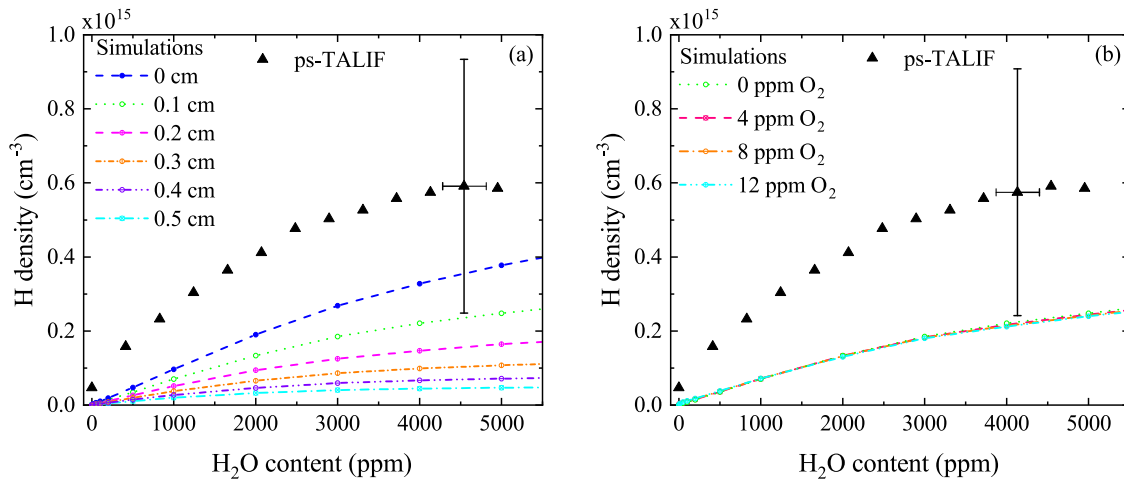


Figure 12. Absolute ground state atomic hydrogen densities as a function of gas humidity content (black triangles). Also shown are simulation results for different distances to the jet nozzle (a), and different air impurity contents (b). Measurements were taken at 500 sccm total gas flow, and 510 V_{pp}. The input power for the simulations is 0.3 W.

5.2. Atomic hydrogen

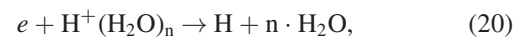
Figure 12 shows measured absolute H densities as a function of H₂O admixture in the feed gas (black triangles) approximately 1 mm from the nozzle of the plasma jet. H densities increase monotonically with increasing humidity content over the whole measurement range.

Similar to figure 9 for atomic oxygen, the dependence of H densities on the distance to the plasma jet nozzle and air impurity content is investigated in the simulations. From figure 12(a) it can be seen that the simulations are predicting lower H densities for all distances. However, simulations of H densities for distances of 0 and 0.1 cm from the plasma jet are closest to the measured values, and within the estimated experimental error. As discussed previously, these distances match best the distance measured in the experiment. Therefore, experiment and simulations are in reasonable agreement. Figure 12(b) shows H densities for different

oxygen impurity contents in the feed gas. From the results it is clear that H densities are almost independent on the amount of impurities in the plasma, in contrast to the trends found for O, where impurities had a large influence on O densities at low water admixtures.

The good agreement between simulation and experiment allows for the investigation of the most important formation pathways for H. The dominant pathways for production and consumption are shown in figures 13 and 14, respectively.

The H production pathways vary strongly with humidity content. At low H₂O admixtures (50 ppm), about 90% of the H production is governed by three reaction mechanisms: (a) collisions of OH and O according to equation (14), (b) destruction of protonated water clusters by recombination with electrons, and (c) two branches of dissociative recombination of H₂O⁺ with electrons



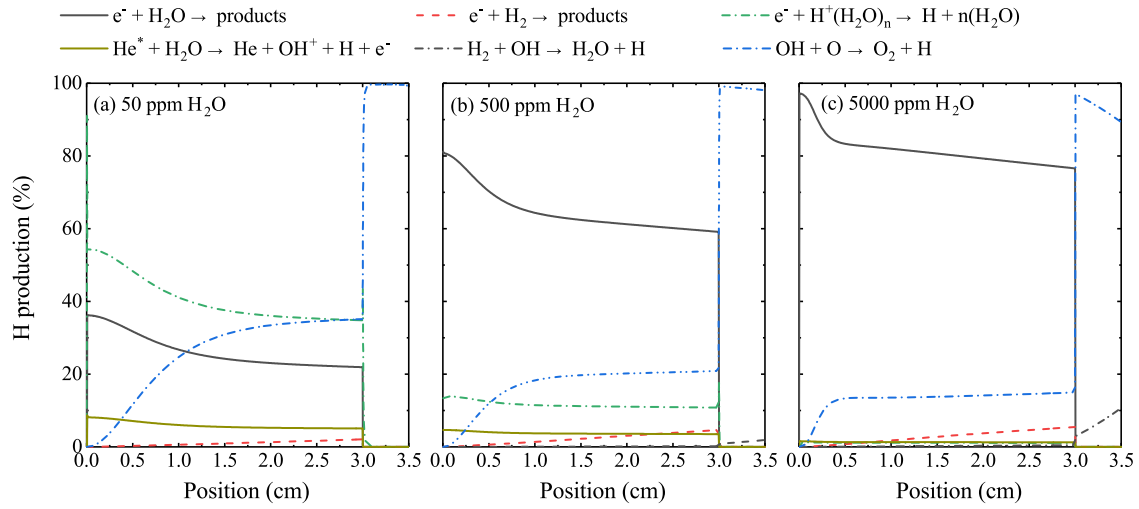


Figure 13. Formation pathways for H at different humidity contents and a fixed O₂ admixture of 8 ppm, 0.3 W and 500 sccm total He flow.

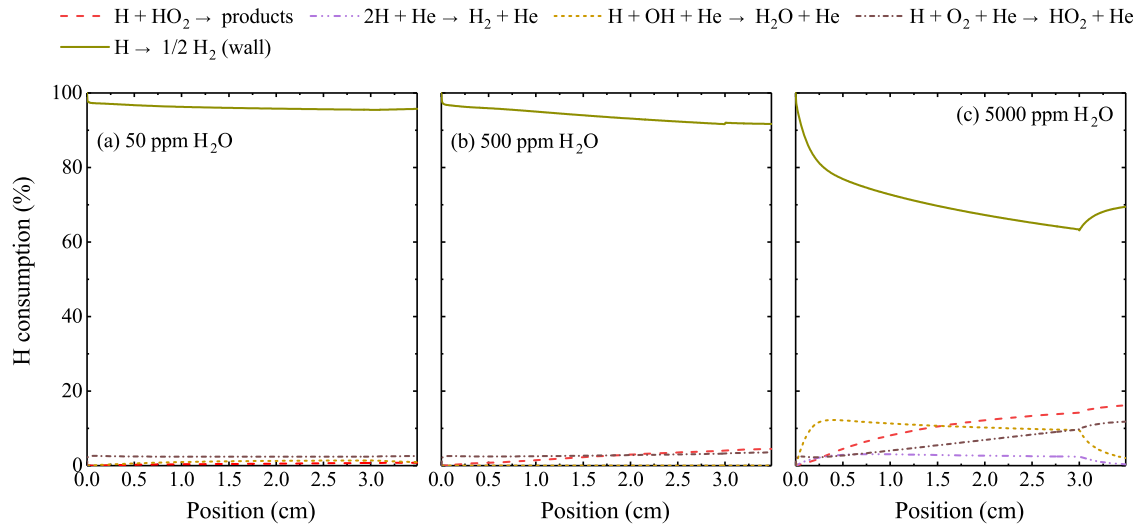
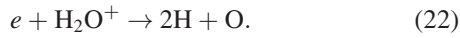
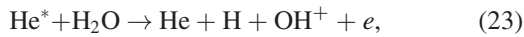


Figure 14. Consumption pathways for H at different humidity contents and a fixed O₂ admixture of 8 ppm, 0.3 W and 500 sccm total He flow.



The remaining 10% contribution comes mainly from Penning ionisation of water molecules and electron impact dissociation of H₂



At high H₂O admixtures (5000 ppm), more than 80% of the H production is through electron impact dissociation of water molecules,



while the remaining contribution is mostly from collisions of OH and O according to equation (14) and to a lesser extent from electron impact dissociation of H₂, equation (24).

For the H₂O content increasing by two orders of magnitude from 50 to 5000 ppm, the density of positive water cluster ions is found to increase by a factor of 6 only. In addition more negative water ion clusters OH⁻(H₂O)_n are formed, leading to an increasing electro-negativity of the plasma. This explains why dissociative recombination of positive H₂O ions and clusters becomes less relevant in comparison to direct electron impact dissociation of H₂O.

As shown in figure 14, the consumption of H is dominated at all humidity contents by recombination at the wall to form H₂



This is reasonable because of the high diffusion coefficient of H atoms, which is inversely proportional to the mass of the particle

$$D = \frac{k_B T_g}{m\nu_m}, \quad (27)$$

where ν_m is the collision frequency. Of course the loss of H to the wall is determined by the surface reaction probability γ_H and the return fraction f_H that is assumed in the simulation. However, as discussed in detail in [77], these coefficients are usually not measured under similar experimental conditions to those used in this work. Their accuracy should therefore be judged carefully. In this work, as discussed in [55, 77], the H surface recombination probability is assumed to be 0.03 for all conditions.

While at low H₂O admixtures, almost all H is consumed by losses to the wall, additional loss mechanisms involving chemical reactions with bulk species become more important at higher H₂O contents. In particular, collisions with OH, HO₂, O₂, and with H itself lead to destruction in the plasma bulk and formation of various short and long-lived species, such as H₂O and H₂.

6. Conclusions

In this work, we investigated the formation of atomic oxygen and hydrogen (O and H) in the COST- μ APPJ in a He-H₂O gas mixture using a combination of two-photon absorption laser-induced fluorescence with picosecond temporal resolution (ps-TALIF), and a global model with a He-H₂O reaction mechanism.

The use of ps-TALIF is motivated by the high collisionality in atmospheric pressure plasmas, leading to short lifetimes of the laser-excited states of O and particularly H. With our setup, we were able to directly measure the effective decay rates and also quenching coefficients of these states with H₂O molecules. These coefficients have not been studied extensively in the literature and therefore this work provides useful additional data for these coefficients. In the case of O, our value lies between two previously measured values, whereas for H, values from the literature are on average a factor 1.5 larger than our value. In this context, we would like to emphasize the crucial advantage of ps-TALIF not to rely on quenching coefficients in the first place, as the effective lifetime, which is necessary for the determination of absolute species densities, is measured separately for each plasma operating condition.

Experimentally determined O densities reach a maximum of $2.0 \times 10^{13} \text{ cm}^{-3}$ at about 3000 ppm at higher humidity contents in the feed gas (≥ 100 ppm). The trend agrees very well with previous work using vacuum VUV-FTAS. Absolute densities are a factor 1.5–2.5, depending on the H₂O content, lower compared to these previous results and results obtained by other groups using nanosecond TALIF.

Crucially, towards very low humidity contents, we find a steep increase of O densities, with a maximum value of $4.3 \times 10^{13} \text{ cm}^{-3}$. This has not been observed in previous investigations, which were carried out in closed systems or in artificial atmospheres. We conclude that these high densities are likely to be produced from O₂ impurities that may originate from a combination of the gas bottle, the gas line and diffusion from ambient air into the gas stream. This trend has been reproduced using a plug-flow, 0D plasma-chemical kinetics model assuming initial feed gas impurities in the order

of ppm. From the simulation we also find that atomic oxygen is mainly produced from O₂ impurities (at low H₂O content) or via reactions between two OH molecules (at high H₂O content), and is consumed via reactions with OH. This also agrees with previous findings. Hence, for reactive species production in plasmas purposely admixed molecules to the feed gas provides a more controllable environment, compared with relying on impurities.

Experimentally determined H densities increase sub-linearly with increasing humidity content up to a density of $6.0 \times 10^{14} \text{ cm}^{-3}$. To our knowledge, no comparable data exists yet in the literature. We find good quantitative and qualitative agreement with the plasma-chemistry model results. Using the model further, we find that the main production pathway for H is via dissociation of protonated water clusters and reactions between OH and O (at low water content) and electron impact dissociation of water (at all water content) and the main consumption pathway to be recombination at the reactor wall, which would highly depend on the assumed surface recombination probability in the simulation.

Since O and H densities show different trends particularly at higher humidity contents (plateau and slight decrease for O, increase for H), changing the humidity content in the plasma yields different O/H ratios. This can be used as a tailoring mechanism for plasma applications.

Acknowledgments




The authors would like to thank Prof Mark J Kushner for providing the GlobalKin code and Richard Armitage for assistance with experimental setups. James Dedrick acknowledges financial support from an Australian Government Endeavour Research Fellowship. This work was financially supported by the UK EPSRC (EP/K018388/1 & EP/H003797/2), and the York-Paris Low Temperature Plasma Collaborative Research Centre. This work is adapted from Chapter 5 of the PhD thesis of Sandra Schröter (Reactive oxygen and hydrogen species generation in radio-frequency atmospheric pressure plasmas - Experimental and numerical investigations, 2017) from the University of York. <http://etheses.whiterose.ac.uk/id/eprint/18738>

Data Availability

The data that support the findings of this study are openly available in the University of York Data Catalog at <http://doi.org/10.15124/61661a76-8e9d-4b45-a86a-6f52191f0de8>

ORCID iDs

Sandra Schröter  <https://orcid.org/0000-0003-1029-4041>
 Andrew R Gibson  <https://orcid.org/0000-0002-1082-4359>
 Andrew West  <https://orcid.org/0000-0003-4553-8640>
 James P Dedrick  <https://orcid.org/0000-0003-4353-104X>
 Erik Wagenaar  <https://orcid.org/0000-0002-5493-3434>

Kari Niemi  <https://orcid.org/0000-0001-6134-1974>
 Timo Gans  <https://orcid.org/0000-0003-1362-8000>
 Deborah O'Connell  <https://orcid.org/0000-0002-1457-9004>

References

- [1] Graves D B 2012 *J. Phys. D: Appl. Phys.* **45** 263001
- [2] Lu X, Naidis G, Laroussi M, Reuter S, Graves D and Ostrikov K 2016 *Phys. Rep.* **630** 1–84
- [3] Dedrick J et al 2017 *J. Phys. D: Appl. Phys.* **50** 455204
- [4] Wijaiakum A et al 2017 *Plasma Sources Sci. Technol.* **26** 115004
- [5] Murakami T, Niemi K, Gans T, O'Connell D and Graham W G 2014 *Plasma Sources Sci. Technol.* **23** 025005
- [6] Murakami T, Niemi K, Gans T, O'Connell D and Graham W G 2013 *Plasma Sources Sci. Technol.* **22** 015003
- [7] Niemi K, O'Connell D, de Oliveira N, Joyeux D, Nahon L, Booth J P and Gans T 2013 *Appl. Phys. Lett.* **103** 034102
- [8] Sousa J S, Niemi K, Cox L J, Algwari Q T, Gans T and O'Connell D 2011 *J. Appl. Phys.* **109** 123302
- [9] Maletić D, Puac N, Lazović S, Malović G, Gans T, Schulz-von der Gathen V and Petrović Z L 2012 *Plasma Phys. Controlled Fusion* **54** 124046
- [10] Turner M M 2016 *Plasma Sources Sci. Technol.* **25** 015003
- [11] Lommatzsch U, Pasedag D, Baalman A, Ellinghorst G and Wagner H E 2007 *Plasma Processes Polym.* **4** S1041–5
- [12] Fang Z, Yang J, Liu Y, Shao T and Zhang C 2013 *IEEE Trans. Plasma Sci.* **41** 1627–34
- [13] Shaw D, West A, Bredin J and Wagenaars E 2016 *Plasma Sources Sci. Technol.* **25** 065018
- [14] Jeong J Y, Babayan S E, Tu V J, Park J, Henins I, Hicks R F and Selwyn G S 1998 *Plasma Sources Sci. Technol.* **7** 282
- [15] Fricke K, Steffen H, von Woedtke T, Schröder K and Weltmann K D 2011 *Plasma Processes Polym.* **8** 51–8
- [16] West A, van der Schans M, Xu C, Cooke M and Wagenaars E 2016 *Plasma Sources Sci. Technol.* **25** 02LT01
- [17] Laroussi M 2009 *IEEE Trans. Plasma Sci.* **37** 714–25
- [18] Park G Y, Park S J, Choi M Y, Koo I G, Byun J H, Hong J W, Sim J Y, Collins G J and Lee J K 2012 *Plasma Sources Sci. Technol.* **21** 043001
- [19] Privat-Maldonado A, O'Connell D, Welch E, Vann R and van der Woude M W 2016 *Sci. Rep.* **6** 35646
- [20] Kong M G, Kroesen G, Morfill G, Nosenko T, Shimizu T, van Dijk J and Zimmermann J L 2009 *New J. Phys.* **11** 115012
- [21] von Woedtke T, Reuter S, Masur K and Weltmann K D 2013 *Phys. Rep.* **530** 291–320
- [22] Bekeschus S, Schmidt A, Weltmann K D and von Woedtke T 2016 *Clin. Plasma Med.* **4** 19–28
- [23] Morfill G E, Kong M G and Zimmermann J L 2009 *New J. Phys.* **11** 115011
- [24] Tipa R S and Kroesen G M W 2011 *IEEE Trans. Plasma Sci.* **39** 2978–9
- [25] Nastuta A V, Topala I, Grigoras C, Pohoata V and Popa G 2011 *J. Phys. D: Appl. Phys.* **44** 105204
- [26] Haertel B, von Woedtke T, Weltmann K D and Lindequist U 2014 *Biomol. Ther.* **22** 477–90
- [27] Isbary G et al 2012 *Br. J. Dermatol.* **167** 404–10
- [28] Lloyd G, Friedman G, Jafri S, Schultz G, Fridman A and Harding K 2010 *Plasma Processes Polym.* **7** 194–211
- [29] Hirst A M, Frame F M, Maitland N J and O'Connell D 2014 *IEEE Trans. Plasma Sci.* **42** 2740–1
- [30] Hirst A M, Simms M S, Mann V M, Maitland N J, O'Connell D and Frame F M 2015 *Br. J. Cancer* **112** 1536–45
- [31] Hirst A M, Frame F M, Arya M, Maitland N J and O'Connell D 2016 *Tumor Biol.* **37** 7021–31
- [32] Gibson A R, McCarthy H O, Ali A A, O'Connell D and Graham W G 2014 *Plasma Processes Polym.* **11** 1142–9
- [33] Ratovitski E A, Cheng X, Yan D, Sherman J H, Canady J, Trink B and Keidar M 2014 *Plasma Processes Polym.* **11** 1128–37
- [34] Mizuno K, Yonetamari K, Shirakawa Y, Akiyama T and Ono R 2017 *J. Phys. D: Appl. Phys.* **50** 12LT01
- [35] Vermeylen S et al 2016 *Plasma Processes Polym.* **13** 1195–205
- [36] Vandamme M et al 2011 *Int. J. Cancer* **130** 2185–94
- [37] Döbele H F, Mosbach T, Niemi K and Schulz-von der Gathen V 2005 *Plasma Sources Sci. Technol.* **14** S31–41
- [38] Zhang S, van Gessel A F H, van Grootel S C and Bruggeman P J 2014 *Plasma Sources Sci. Technol.* **23** 025012
- [39] van Gessel A F H, van Grootel S C and Bruggeman P J 2013 *Plasma Sources Sci. Technol.* **22** 055010
- [40] Wagenaars E, Gans T, O'Connell D and Niemi K 2012 *Plasma Sources Sci. Technol.* **21** 042002
- [41] Schröder D, Bahre H, Knake N, Winter J, de los Arcos T and Schulz-von der Gathen V 2012 *Plasma Sources Sci. Technol.* **21** 024007
- [42] Hänsch T W, Lee S A, Wallenstein R and Wieman C 1975 *Phys. Rev. Lett.* **34** 307
- [43] Bischel W K, Perry B E and Crosley D R 1981 *Chem. Phys. Lett.* **82** 85–8
- [44] Bokor J, Freeman R R, White J C and Storz R H 1981 *Phys. Rev. A* **24** 612
- [45] Kulatilaka W D, Gord J R, Katta V R and Roy S 2012 *Opt. Lett.* **37** 3051
- [46] Winter J, Brandenburg R and Weltmann K D 2015 *Plasma Sources Sci. Technol.* **24** 064001
- [47] Dvorák P, Talába M, Obrusník A, Kratzer J and Dědina J 2017 *Plasma Sources Sci. Technol.* **26** 085002
- [48] Mrkvičková M, Ráhel J, Dvořák P, Trunec D and Morávek T 2016 *Plasma Sources Sci. Technol.* **25** 055015
- [49] Kondeti V S S K, Zheng Y, Luan P, Oehrlein G S and Bruggeman P J 2020 *J. Vac. Sci. Technol., A* **38** 033012
- [50] Yatom S, Luo Y, Xiong Q and Bruggeman P J 2017 *J. Phys. D: Appl. Phys.* **50** 415204
- [51] Yue Y, Kondeti V S S K and Bruggeman P J 2020 *Plasma Sources Sci. Technol.* **29** 04LT01
- [52] Schmidt J B, Sands B L, Kulatilaka W D, Roy S, Scofield J and Gord J R 2015 *Plasma Sources Sci. Technol.* **24** 032004
- [53] Schmidt J B, Roy S, Kulatilaka W D, Shkurenkov I, Adamovich I V, Lempert W R and Gord J R 2016 *J. Phys. D: Appl. Phys.* **50** 015204
- [54] Schmidt J B, Sands B, Scofield J, Gord J R and Roy S 2017 *Plasma Sources Sci. Technol.* **26** 055004
- [55] Frank J H and Settersten T B 2005 *Proc. Combust. Inst.* **30** 1527–34
- [56] Golda J et al 2016 *J. Phys. D: Appl. Phys.* **49** 084003
- [57] Schröter S et al 2018 *Phys. Chem. Chem. Phys.* **20** 24263
- [58] Bischoff L et al 2018 *Plasma Sources Sci. Technol.* **27** 125009
- [59] Alduchov O A and Eskridge R E 1996 *J. Appl. Meteorol.* **35** 601–9
- [60] Benedikt J, Schröder D, Schneider S, Willems G, Pajdarová A, Vlček J and Schulz-von der Gathen V 2016 *Plasma Sources Sci. Technol.* **25** 045013
- [61] Niemi K, Schulz-von der Gathen V and Döbele H F 2001 *J. Phys. D: Appl. Phys.* **34** 2330–5
- [62] Niemi K, Schulz-von der Gathen V and Döbele H F 2005 *Plasma Sources Sci. Technol.* **14** 375–86
- [63] Kramida A, Yu R and Reader J (NIST ASD Team) 2016 *NIST Atomic Spectra Database (ver. 5.3)*, [Online] available: <http://physics.nist.gov/asd> Gaithersburg, MD National Institute of Standards and Technology
- [64] Boogaarts M G H, Mazouffre S, Brinkman G J, van der Heijden H W P, Vankan P, van der Mullen J A M, Schram D C and Döbele H F 2002 *Rev. Sci. Instrum.* **73** 73–86

- [65] Reuter S, Niemi K, Schulz-von der Gathen V and Döbele H F 2009 *Plasma Sources Sci. Technol.* **18** 015006
- [66] Horiguchi H 1981 *J. Chem. Phys.* **75** 1207–18
- [67] Condon E U and Shortley G H 1951 *Theory of Atomic Spectra* (Cambridge: Cambridge University Press)
- [68] Preppernau B L, Pearce K, Tserepi A, Wurzberg E and Miller T A 1995 *Chem. Phys.* **196** 371–81
- [69] West A 2016 Optical and electrical diagnostics of atmospheric pressure plasma jets *PhD Thesis* University of York
- [70] Chang R S F, Horiguchi H and Setser D W 1980 *J. Chem. Phys.* **73** 778–90
- [71] Marinov D, Drag C, Blondel C, Guaitella O, Golda J, Klarenaar B, Engeln R, Schulz-von der Gathen V and Booth J P 2016 *Plasma Sources Sci. Technol.* **25** 06LT03
- [72] Hurlbatt A, Gibson A R, Schröter S, Bredin J, Foote A P S, Grondein P, O'Connell D and Gans T 2016 *Plasma Processes Polym.* **14** 1600138
- [73] Lietz A M and Kushner M J 2016 *J. Phys. D: Appl. Phys.* **49** 425204
- [74] Quickenden T I, Trotman S M, Irvin J A and Sangster D F 1979 *J. Chem. Phys.* **71** 497–501
- [75] Meier U, Kohse-Höinghaus K and Just T 1986 *Chem. Phys. Lett.* **126** 567–73
- [76] Bittner J, Kohse-Höinghaus K, Meier U and Just T 1988 *Chem. Phys. Lett.* **143** 571–6
- [77] Schröter S, Gibson A R, Kushner M J, Gans T and O'Connell D 2018 *Plasma Phys. Controlled Fusion* **60** 014035
- [78] Waskoenig J, Niemi K, Knake N, Graham L M, Reuter S, Schulz-von der Gathen V and Gans T 2010 *Plasma Sources Sci. Technol.* **19** 045018